Ultrasonics - Sonochemistry 61 (2020) 104836

Contents lists available at ScienceDirect

Ultrasonics - Sonochemistry

journal homepage: www.elsevier.com/locate/ultson

Sonochemical synthesis of Dy^{3+} substituted $Mn_{0.5}Zn_{0.5}Fe_{2-x}O_4$ nanoparticles: Structural, magnetic and optical characterizations

M.A. Almessiere[a,b], Y. Slimani[a,*], A. Demir Korkmaz[c], S. Güner[d], A. Baykal[e], S.E. Shirsath[f], I. Ercan[a], P. Kögerler[d]

[a] Department of Biophysics, Institute for Research & Medical Consultations (IRMC), Imam Abdulrahman Bin Faisal University, P.O. Box 1982, 31441 Dammam, Saudi Arabia
[b] Department of Physics, College of Science, Imam Abdulrahman Bin Faisal University, P.O. Box 1982, 31441 Dammam, Saudi Arabia
[c] Department of Chemistry, Istanbul Medeniyet University, 34700 Uskudar-Istanbul, Turkey
[d] Institute of Inorganic Chemistry, RWTH Aachen University, 52074 Aachen, Germany
[e] Department of Nano-Medicine Research, Institute for Research & Medical Consultations (IRMC), Imam Abdulrahman Bin Faisal University, P.O. Box 1982, 31441 Dammam, Saudi Arabia
[f] School of Materials Science and Engineering, University of New South Wales, Kensington, Sydney, NSW 2052, Australia

ARTICLE INFO

Keywords:
Mn-Zn ferrite
Rare earth
Structure
Optical properties
Magnetization
AC susceptibility
ZFC-FC

ABSTRACT

$Mn_{0.5}Zn_{0.5}Dy_xFe_{2-x}O_4$ ($x \leq 0.03$) nanoparticles (NPs) were fabricated by using Ultrasonic irradiation using UZ SONOPULS HD 2070 ultrasonic homogenizer (frequency of 20 kHz and power of 70 W). Structural and morphological analyses were performed via XRD (X-ray powder diffractometer), TEM (Transmission electron microscopy) and SEM (Scanning electron microscopy). XRD presented the formation of Mn-Zn ferrite with average crystal size in 11 to 18 nm range. Direct optical energy band gaps (E_g) were specified applying diffuse reflectance investigations. E_g values are in a small band range of 1.61–1.67 eV. Low (10 K) and room temperature VSM data were recorded applying ± 90 kOe external magnetic field. All samples exhibit superparamagnetic properties at RT. Magnetization parameters significantly increase due to coordination of Dy^{3+} rare earth ions. Magnetic moment per molecule (n_B) increases from 0.952 μ_B to 1.137 μ_B and from 2.312 μ_B to 2.547 μ_B at RT and at 10 K data respectively. 10 K coercivity (H_c) values decrease from 260 Oe to 43 Oe. All samples have squareness ratios (SQR) of 0.231–0.400 range assigning the multi-domain structure at 10 K. ZFC-FC magnetization curves that were registered for two selected samples exhibit a divergence and a sharp drop below their T_{peak} positions. This event is typically correlated to the collective freezing of system and spin-glass-like phase. Real part AC susceptibility data slightly shift toward high temperature regions with increasing frequencies. Critical Slowing Down (CSD) model explained the spin dynamics of interacting NPs consistently with literature and proved the spin-glass behavior of samples at low temperatures.

1. Introduction

Nowadays, spinel ferrites are being widely explored because of their versatile physio-chemical properties. These ferrites have wide range of applications including telecommunication, microwave absorbers, magnetic storage, military devices, etc [2,3]. Among those, manganese zinc ferrite (MZF) nanoparticles (NPs) are soft magnetic materials with microwave absorption, large initial permeability, high electrical resistivity, great magnetic saturation and low energy loss [1]. Thus, MZFs are widely used as converters, inductor cores, magnetic electromagnetic wave absorbers and recording heads in technological applications such as electromagnetic interference (EMI) suppression, data transmission circuitry, spintronic devices [2–7]. In addition, they are ideal candidates for catalysis especially in environmental applications [8,9], and drug delivery and magnetic hyperthermia agents in biomedicine [2,10]. Zn ferrite is a normal ferrite however Mn ferrite displays a mixed spinel structure. So, as the amount of zinc ion increases, it is expected the structure to display more characteristics of a normal spinel and vice versa. So, it is the interactions of cations at the sublattices and interstitial sites which determine the structural, electrical and magnetic properties of spinel ferrites. Thus, it could tune the magnetic characteristics of MZFs can be changed by the incorporation of different cations by the crystal structure of MZF NPs.

Rare earth metal (RE) ions with large ionic radii exhibit high

* Corresponding author.
E-mail address: yaslimani@iau.edu.sa (Y. Slimani).

https://doi.org/10.1016/j.ultsonch.2019.104836
Received 29 July 2019; Received in revised form 11 October 2019; Accepted 21 October 2019
Available online 23 October 2019

magnetostriction, magnetic moments and magneto-crystalline anisotropy at low temperatures owing to the higher spin–orbit coupling in their 4*f* electrons. Again, the RE ions with bigger ionic radii can give rise to distortions in the crystal structure and the magnetic coercivity [11]. Hence, the substitution of trivalent iron ions with RE ions in MZF can enhance magnetic and optical characteristics of these ferrites. There have been many studies on the incorporation of RE ions to MZFs in the literature. In one study, the permeability was enhanced while the magnetic loss and the coercivity was reduced by the incorporation of Ce_2O_3, Gd_2O_3, Sm_2O_3, or Y_2O_3 to MZFs by solid state synthesis route. The single phased crystal structure was maintained up to 0.07 wt% doping. For enhancing the magnetic properties, the optimum doping amount was 0.01 wt% in Gd_2O_3 and Sm_2O_3, and 0.03 wt% in Ce_2O_3, and Y_2O_3 [12]. Angadi et al. stated that an increase in the Sc^{3+} concentration up to x = 0.03 in $Mn_{0.5}Zn_{0.5}Sc_yFe_{2-x}O_4$ NPs which were prepared by a solution combustion technique increased magnetic characteristics such as magnetic moment (n_B), magnetic particle size (D_m), M_s, and remanent magnetization (M_r); and decreased the frequency dependent dielectric constant as well as the dielectric constant [13]. Finally, Thakur and co-workers have investigated the effect of La^{3+} substitution in MZF NPs ($Mn_{0.5}Zn_{0.5}La_xFe_{2-x}O_4$) prepared with co-precipitation. The *Ms* and η_B of the NPs increased again up to x = 0.05 while the crystallite size showed a minimum at this concentration. When x > 0.05, $LaFeO_3$ phase was observed in XRD diffractograms indicating the solubility limit of the large lanthanum ion in MZF being x = 0.05 for the above composition and formation of multi-domains in the structure. In addition, the authors concluded that there was a maximum tendency of lanthanum ions in Oh sites to substitute the ferric ions for x = 0.050, at which a superparamagnetic behavior was observed [14]. All these methods may present some advantages such as controlling the crystal size and dispersion however, they suffer from drawbacks which require large amounts of solvents which may be toxic to the health, or damage the environment, sintering at high temperatures, and complicated procedures. Therefore, an alternative synthesis route should be provided to synthesize RE-substituted MZF NPs without such disadvantages.

Ultrasonic cavitation chemistry or sonochemical method has been presented as a greener and faster technique for the preparation of MZF NPs as well as other magnetic materials. The ultrasonic irradiation offers a much shorter reaction time by reaching extremely high pressures (20 MPa) and temperatures (~5000 K) in addition to a rapid cooling rate (~10^{10} per second) by the creation and downfall of cavitation bubbles in liquid systems [15]. Furthermore, the hydrolysis rate is highly enhanced, and the sonochemical synthesis route can obtain NPs with a more uniform size distribution and higher phase purity [16].

Therefore, in this study, we accounted on the synthesis of $Mn_{0.5}Zn_{0.5}Dy_xFe_{2-x}O_4$ (x ≤ 0.03) NPs obtained with ultrasonic irradiation. The goal of our research is to explore the influence of Dy^{3+} doping on magnetic and optical properties of $Mn_{0.5}Zn_{0.5}Fe_2O_4$ NPs fabricated by sonochemical method.

2. Experimental and instrumentation

Ultrasonic irradiation was implemented to synthesis $Mn_{0.5}Zn_{0.5}Dy_xFe_{2-x}O_4$ (x ≤ 0.03) NPs. Series of metal salts: manganese (II) chloride ($MnCl_2{\cdot}4H_2O$), zinc(II) nitrate ($Zn(NO_3)_2$), dysprosium(III) nitrate hydrate ($Dy(NO_3)_3$) and iron (III) nitrate nonahydrate (($Fe(NO_3)_3{\cdot}9H_2O$) were mixed together in deionized water and the pH was adjusted to 11 by adding a drop wise of 3 M NaOH solution, then the final solution was subjected to ultrasonic irradiation (UZ SONOPULS HD 2070; 20 kHz and 70 W) with high-intensity for 45 min. After that, the solution was washed several times with deionized water and the magnetic solid part was parted magnetically. Finally, powdered sample was dried at 80 °C for further analysis.

Rigaku Benchtop Miniflex X-ray diffraction (XRD) powder diffractometry with CuK_α radiation (λ = 1.5406 Å) has been employed to verify the structure of prepared compositions. XRD patterns were done in 2θ angle range of 20−70° with a step of 0.02°. The microstructure was evaluated by SEM (FEI Titan ST) along with EDX system and TEM (FEI Morgagni 268). The Bruker FT-IR was utilized for spectral investigation. Quantum Design-PPMS Dyna Cool system worked in temperature range between 2 and 400 K was utilized for, magnetization, AC magnetic susceptibility, and ZFC-FC magnetization measurements.

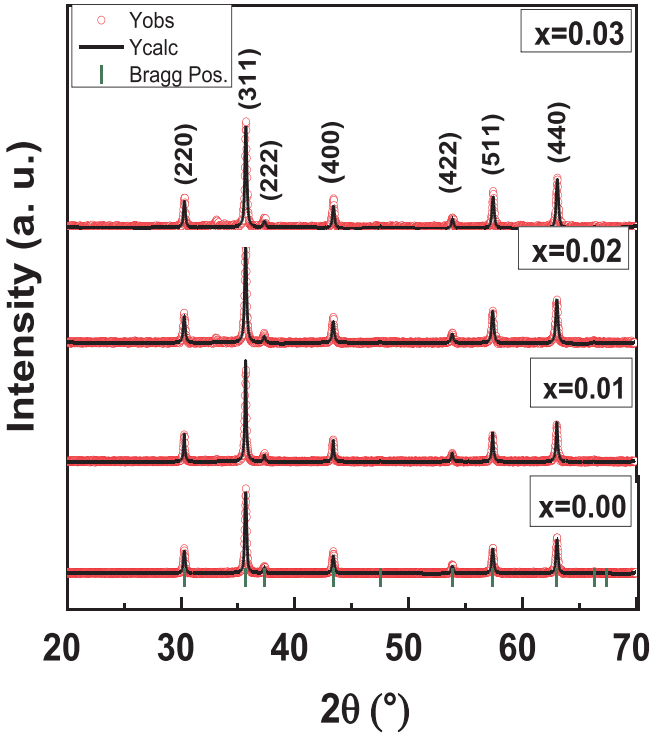

Fig. 1. XRD powder patterns of $Mn_{0.5}Zn_{0.5}Dy_xFe_{2-x}O_4$ (x ≤ 0.03) NPs.

3. Results and discussion

3.1. Structural identification

The spinel phase of $Mn_{0.5}Zn_{0.5}Dy_xFe_{2-x}O_4$ (x ≤ 0.03) NPs have been authenticated by X-ray diffractometer as shown in Fig. 1. All XRD patterns of the compositions are clearly belong to Mn-Zn cubic spinel ferrite without presence to any unidentified peaks. The X-ray diffraction peaks exhibited a broaden indicative of smaller crystalline size. The structural constants are executed via Rietveld refinement with Fullproof software method. It is apparent that there is a remarkable increasing in lattice constants with increasing the Dy^{3+} ratio resulted from the expansibility in unit cell of spinel crystal by subtitling larger ionic radii ions that caused a lattice micro-strains which generates internal stresses [17]. The average crystallites size was calculated by means of Debye–Scherrer equation as follow [18]:

$$D_{XRD} = \frac{0.9\lambda}{\beta cos\theta} \quad (1)$$

where λ is the wavelength of CuKα radiation and β is the peaks width at half maximum intensity. The crystallites sizes are found in the range 11 to 18 nm.

Well-known Bertaut approach [19] was used to determine the cations distribution in $Mn_{0.5}Zn_{0.5}Dy_xFe_{2-x}O_4$ ferrite system. The ratio of I_{220}/I_{440} and I_{422}/I_{400} XRD lines were used for the calculations since they are assumed to be sensitive to the cation distribution (Table 1) [20,21]. Mn^{2+} ions are considered to occupy 20% and 80% of the O_h and T_d sites, respectively [20], which is not true in the present case where Mn^{2+} ions are distributed as 60% and 40% over the O_h and T_d

Table 1
Structural parameters and Cation distribution of $Mn_{0.5}Zn_{0.5}Dy_xFe_{2-x}O_4$ ($x \leq 0.03$) NPs.

x	a (Å)	V (Å)^3	D_{XRD} (nm) ± 0.10	χ^2(chi^2)	R_{Bragg}	Cation distribution	
						T_d A-site	O_h B-site
0.00	8.4119	595.22	11.0	1.85	23.3	$Mn_{0.2}Zn_{0.5}Fe_{0.3}$	$Mn_{0.3}Fe_{1.7}$
0.01	8.4121	595.25	11.9	1.59	33.3	$Mn_{0.2}Zn_{0.5}Fe_{0.3}$	$Mn_{0.3}Dy_{0.01}Fe_{1.69}$
0.02	8.4281	598.67	15.8	1.01	16.6	$Mn_{0.2}Zn_{0.5}Fe_{0.3}$	$Mn_{0.3}Dy_{0.02}Fe_{1.68}$
0.03	8.4410	601.42	18.2	2.5	31.1	$Mn_{0.2}Zn_{0.5}Fe_{0.3}$	$Mn_{0.3}Dy_{0.03}Fe_{1.67}$

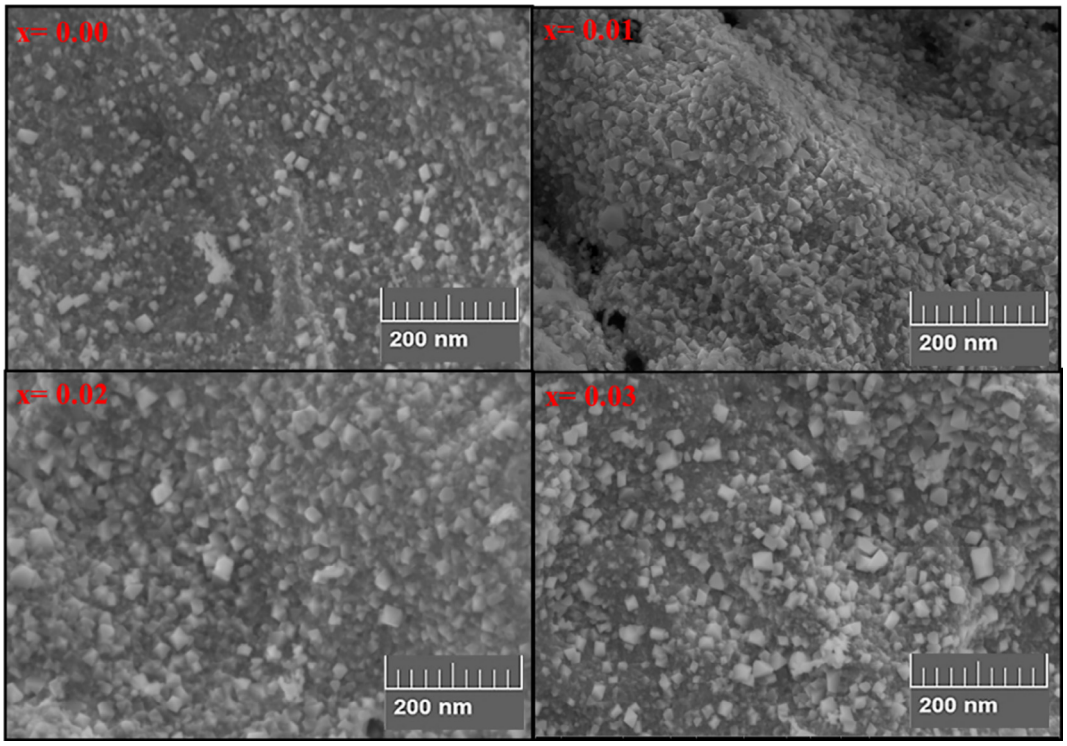

Fig. 2. SEM micrographs of Dy^{3+} ions substituted MZF NPs.

sites, respectively. This is due to the dominancy of Zn^{2+} ions to occupy the T_d site. The Fe^{3+} ions content at the O_h site reduced with the increase in "x" which occupy O_h site as well.

3.2. SEM, TEM and EDX analysis

Fig. 2 displayed the SEM images of $Mn_{0.5}Zn_{0.5}Dy_xFe_{2-x}O_4$ ($x \leq 0.03$) NPs. The images revealed a regular size and uniform distribution of cubic particles with aggregation. The average particles size is less than 20 nm and is growing with increasing the Dy content. Similarly, the TEM images of $Mn_{0.5}Zn_{0.5}Dy_xFe_{2-x}O_4$ ($x = 0.01$ and 0.02) NPs as seen in Fig. 4 showed an agglomeration of cubic nanoparticles because of the magnetic interaction among nanoparticles. SAED patterns and size distribution histograms established the formation of Mn-Zn spinel ferrite structure with a particle size below 20 nm, which accord with XRD analyses. Fig. 3 presented the EDX and elemental mapping of $Mn_{0.5}Zn_{0.5}Dy_xFe_{2-x}O_4$ ($x = 0.01$ and 0.03) NPs. It showed the characteristic peaks of the following elements Mn, Zn, Dy, Fe and O without any impurities. EDX presented the values of weight percentage experimentally and theoretically that confirmed the formation of the desired compositions. These data support the XRD data that the main composition is constructed.

3.3. FT-IR

FT-IR spectra of $Mn_{0.5}Zn_{0.5}Dy_xFe_{2-x}O_4$ ($x \leq 0.03$) NPs were presented in Fig. 5. FT-IR spectra of spinel ferrites consist of two characteristic stretching vibrations corresponding to intrinsic vibration of the metal complex; including bonds between oxygen ions and metal cations in tetrahedral (T_d) and octahedral (O_h) sites in the range of 400–600 cm^{-1} [22]. The band observed at the higher wave number ν_1 (~600 cm^{-1}) is assigned to M_{tetra}–O stretching vibration, while the band at the lower wave number ν_2 (~410 and 460 cm^{-1}) is attributed to the stretching vibration of M_{octa}–O bonds of spinel ferrite. The bands in the range of 400–410 cm^{-1} are related to octahedral-metal stretching vibration of Co-O bonds. While, the bands at ~460 and ~600 cm^{-1} are attributed to octahedral- and tetrahedral- metal stretching vibrations of Fe-O bonds [23].

3.4. Optical study

Percent diffuse reflectance UV–vis (PDR-UV–vis) spectroscopic measurements were conducted to reveal the optical properties of $Mn_{0.5}Zn_{0.5}Dy_xFe_{2-x}O_4$ ($x \leq 0.03$) NPs. Fig. 6.a shows the PDR (or also abbreviated as DRS) data that were documented in the 200–800 nm range of incident light. Photon energies from 1.55 to 6.2 eV correspond to a whole sweep region of applied radiation. Reflectance intensities of spectra form narrow band between 13% and 15% for the initial half of whole sweep region that is between 200 nm and 500 nm. Sharp increases are observed at all reflectance intensities until a maximum 25% for the second half of sweep range.

The analyses on reflectance spectra are based on Kubelka-Munk (K-

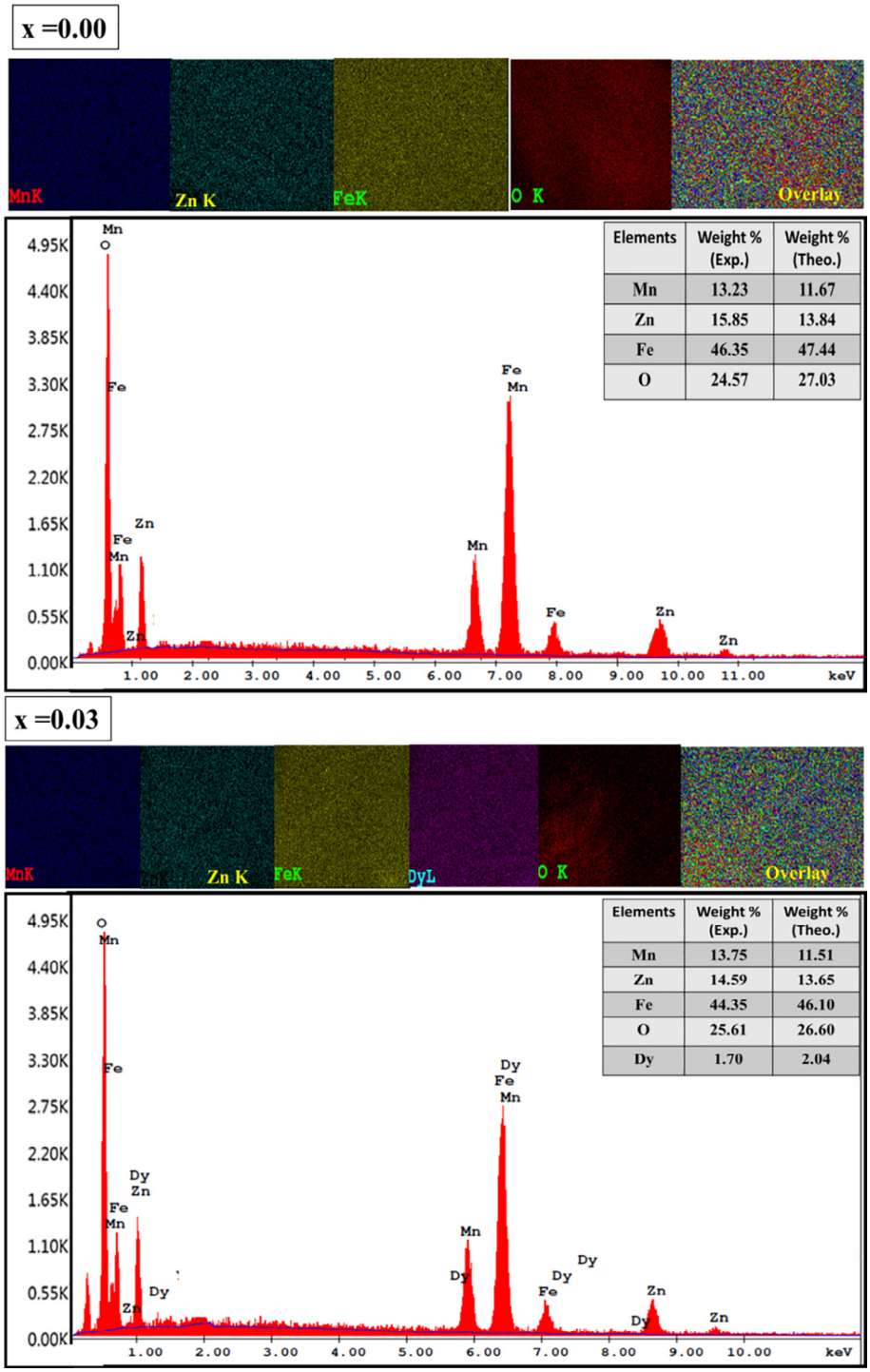

Fig. 3. EDX spectra and elemental mapping of x = 0.00 and 0.03 compositions.

M) theory and a function, $F(R_\infty)$ is demarcated as below:

$$F(R_\infty) = \frac{(1-R_\infty)^2}{2R_\infty} = \frac{K}{S} = \frac{2.303\varepsilon C}{S} \quad (2)$$

where, reflectance of infinitely thick sample, R_∞; absorptivity, ε; absorption coefficient, K; scattering coefficient, S; analyte concentration, C. It is understood from Eq. (2) that K-M theory is a two-constant theory: reflectance characteristics are related to the ratio of the absorption to scattering coefficients (K/S) that are the two constants [24]. Optical energy band gap (E_g) of samples are estimated via Tauc equation that correlates the $F(R_\infty)$ and E_g [25–27],

$$(F(R_\infty)h\upsilon)^n = A(h\upsilon - E_g) \quad (3)$$

here, A is a constant, $h\upsilon$ is the energy of incident radiation, and power $n = 2$ represents the direct electronic transition. E_g values can be estimated by plotting $(F(R_\infty)h\upsilon)^2$ versus $(h\upsilon)$ graphs. An extrapolated straight fit line to the linear part of graph intercepts the energy axis for $(F(R_\infty)h\upsilon)^2 = 0$, then the corresponding value on energy axis is ascribed as E_g in units of eV. Fig. 6(b-e) contains the Tauc plots and estimated E_g values of all products. Dy^{3+} undoped $Mn_{0.5}Zn_{0.5}Fe_2O_4$ has 1.67 eV E_g value. Doped samples have band gap magnitudes of 1.64 eV, 1.64 eV and 1.61 eV corresponding to Dy^{3+} ion ratios of x = 0.01, 0.02, and 0.03, respectively. Hence, the Dy^{3+} ion doping does not cause

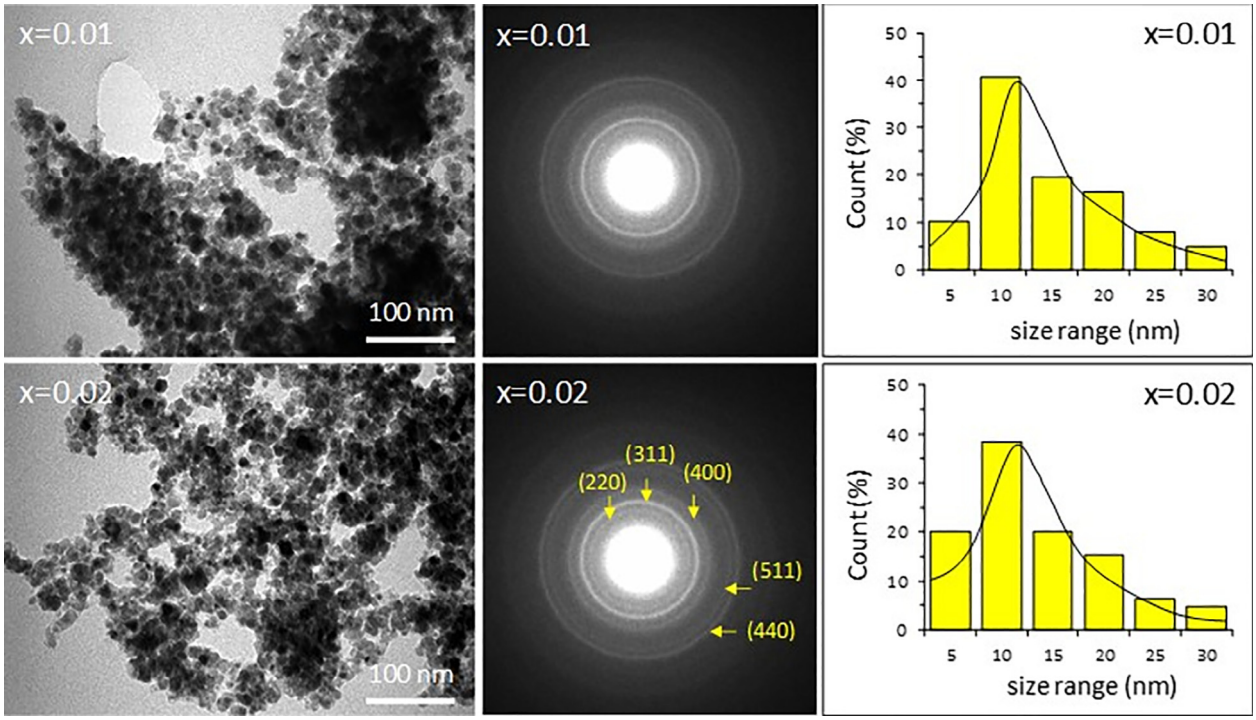

Fig. 4. TEM images, SAED patterns and size distribution histograms of x = 0.01 and 0.02 compositions.

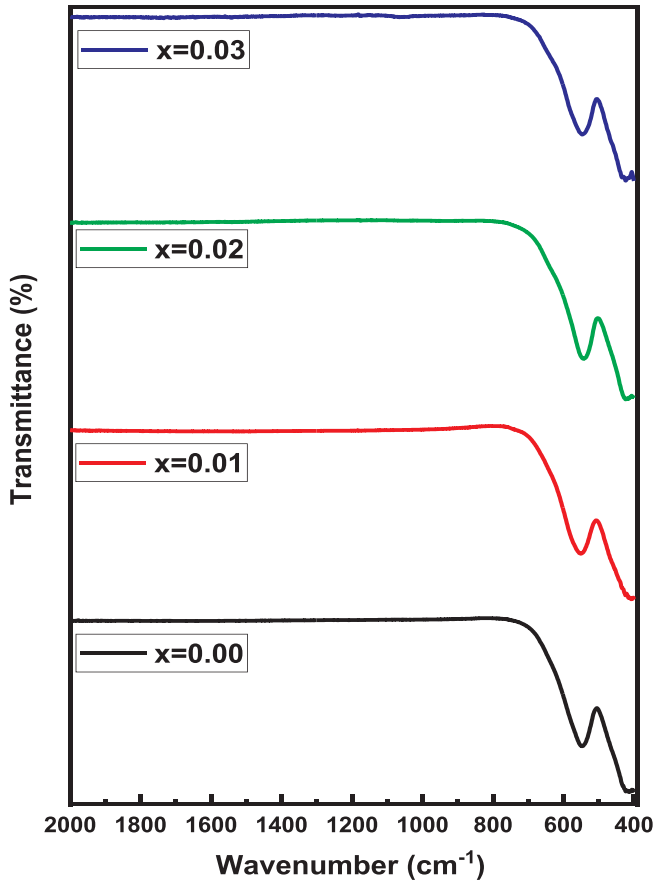

Fig. 5. FT-IR spectra of $Mn_{0.5}Zn_{0.5}Dy_xFe_{2-x}O_4$ (x ≤ 0.03) NPs.

significant changes at the direct E_g of mixed spinel ferrite sample. All assessed data are in the semiconductor band gap range. Nam and Ashok groups stated the 1.98 eV and 1.99 eV of direct E_g values for mixed $Mn_{0.5}Zn_{0.5}Fe_2O_4$ NPs which were synthesized via hydrothermal and sonication assisted microwave irradiation methods, respectively [28,29]. Reported average D_{XRD} sizes by these two groups are 14 nm and 9.4 nm, respectively. One can say that there is the same magnitude of band gap although different sizes. In addition, our group had reported E_g data between 1.86 eV and 2.80 eV for varying concentrations of mixed $Mn_{1-x}Zn_xFe_2O_4$ (x = 0.2–0.8) ferrites which were produced by citric acid assisted sol–gel and thermal decomposition processes [30,31]. We also reported E_g data for SiO_2 coated $Mn_{1-x}Zn_xFe_2O_4$ nanoparticles [32]. According to our investigations, we cannot see a direct correlation between crystallite sizes and band gaps. That is why, we interpret as that in addition to particle size, geometry, synthesis method and coated shell types also play significant role at band gap of Mn-Zn including ferrite samples. However, there is no reported E_g data directly about Dy^{3+} doped $Mn_{0.5}Zn_{0.5}Fe_2O_4$ NPs in the literature.

3.5. Magnetization

Hysteresis loops M(H) versus applied magnetic field were recorded as initial phase. The magnetic measurements are implemented at RT and at 10 K with magnetic field of ± 90 kOe. Fig. 7 presents magnetization curves belong to all samples at RT. The curves at RT have S-like shape assigning the superparamagnetic nature of mixed and doped samples [33]. Although very high magnitude of applied external field, M_s data were extrapolated from the linear fits of M vs. $1/H^2$ plots and they were presented in Fig. 7 as inset [34,35]. It was found that the M_s of undoped sample increases with increasing Dy^{3+} ratios from 22.51 to 26.59 emu/g at RT. When the magnetic moments of ions are compared, the substitution of Dy^{3+}(10.63 μ_B) for Fe^{3+} (5 μ_B) is expected to enhance the magnetization as we observed. Additionally, the substitution of Fe^{3+} (0.62 Å) ions by Dy^{3+} (1.07 Å) ions having larger ionic radii reduces the distances between magnetic ions, which causes to strengthening of A-B exchange interactions. Moreover, all rare-earth ions cannot enter into the spinel lattice, because of their larger radii. Consequently, some RE^{3+} ions might accumulate at grain boundary and form isolating ultra-thin layer around the grains during the sintering process [36]. This may increase the magnitude of magnetic

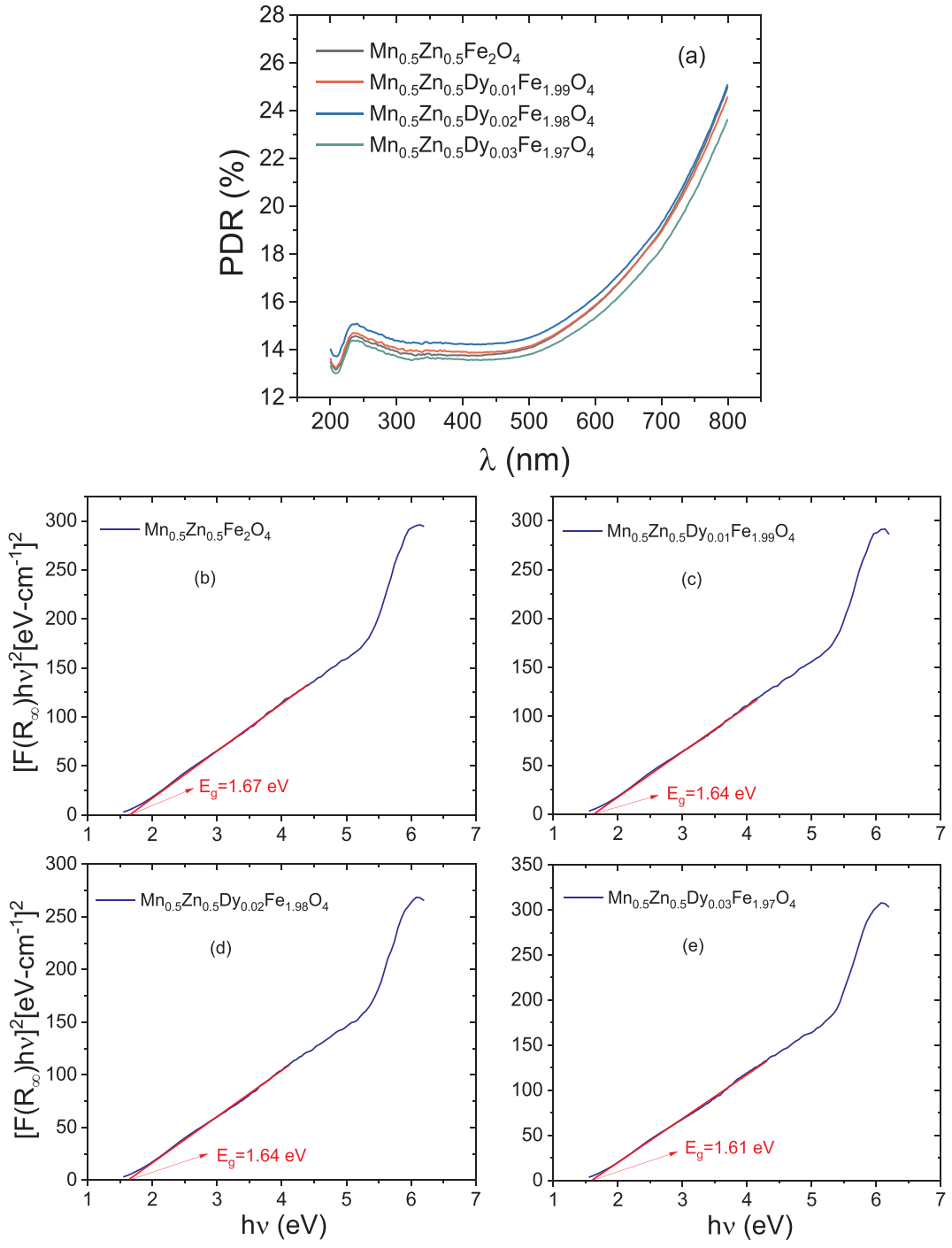

Fig. 6. (a) PDR spectra (b), (c), (d) and (e) Tauc plots of $Mn_{0.5}Zn_{0.5}Dy_xFe_{2-x}O_4$ (x ≤ 0.03) NPs.

interactions and cause the increase of M_s. Furthermore, the variation in the values of the magnetic moment (n_B) could explain the behavior of M_s. It is well known that the strengthening of the exchange interactions among the A and B sites in ferrites lead to an increase in n_B values.

If magnetic anisotropy of each particle in the assembly has no anisotropy, then the magnetic moment of each particle can point in any direction, and the classical theory of paramagnetism applies. Hence, magnetization curves of samples in the superparamagnetic state can be correlated with the size dependent Langevin function. It is also possible to estimate the diameter of magnetically active core of nanoparticles [35].

$$M(d.\ H) = \sum M_i f(d_i) L(\alpha_i) \tag{4}$$

where, M_i magnetization of i^{th} particle, and $f\ (d_i)$ log normal distribution function, which is expressed as:

$$f(d_i) = \frac{1}{\sqrt{2\pi}\ln\sigma} exp\left\{-\frac{(lnd_i - lnd_m)^2}{2ln^2\,\sigma}\right\} \tag{5}$$

where, $d_m$statistical median, d_i diameter of i^{th} particle, σ geometric standard deviation. The Langevin function is given

$$L(\alpha_i) = [\coth(\alpha_i) - 1/\alpha_i] \text{with} \alpha_i = \frac{M_s VH}{k_B T} \tag{6}$$

This expression takes the log-normal particle size distribution into account; not the diameter of nanoparticles [37].

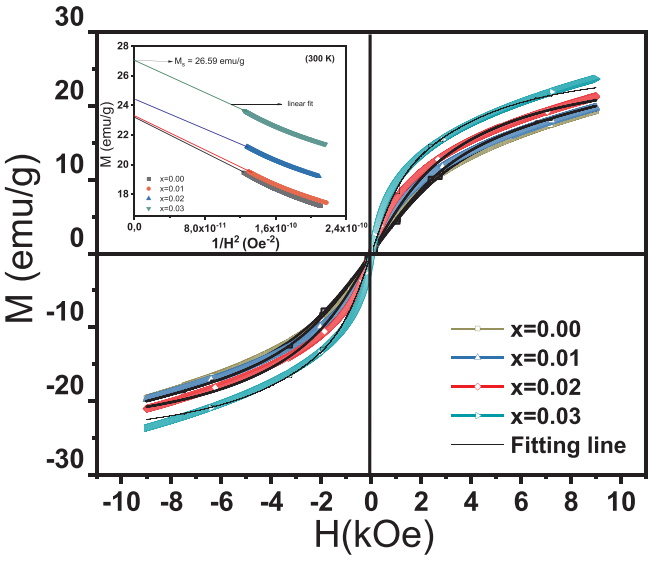

Fig. 7. M-H curves of $Mn_{0.5}Zn_{0.5}Dy_xFe_{2-x}O_4$ (x ≤ 0.03) NPs at RT, *M* against $1/H^2$ plots are as inset.

$$D_{mag} = \frac{\sum_1^n d_i f(d_i)}{n} \quad (7)$$

V is the volume of fully magnetic core assumed to have spherical shape, $V = \frac{\pi D_M^3}{6}$ while D_{mag} is the value of average magnetic diameter that is calculated using fit parameters and Eq. (7). Magnetic core sizes are between 15.64 and 20.87 nm as listed in Table 2. These dimensions are in accordance with the D_{XRD}values. We calculated experimental magnetic moment per molecule, n_B in units of μ_B for samples by using the general expression $n_B = Molecularweight x \sigma_s/5585$. n_B values increases from 0.952 μ_B to 1.137 μ_B with increasing Dy^{3+} content because of the direct correlation with increasing M_s at RT.

When ferro or ferrimagnetic NPs have a size smaller than critical diameter then coercivity is zero and thermal effects are strong enough to prevent spontaneous magnetization. Magnetization measurements performed at very low temperatures (like 10 K) could elucidate the internal anisotropic properties of NPs. Such as, NPs can exhibit internal coercivities (H_{ci}) in the case of enough magnitude of magneto-crystalline anisotropy constant (K) due to excluded negative effects of heat. Here H_{ci} (or H_a) is a particular value of the true field H acting on the nanocrystal, where H is the sum of the externally applied field and the demagnetizing field. Hence, magnetic hysteresis curves recorded at 10 K are given in the Fig. 8(a) and (b). The detected M_r (remanent magnetization) and H_c (coercivity) data exhibit the ferrimagnetic nature of measured samples at 10 K, especially clear view in Fig. 8(b). M_s values were estimated as increasing from 54.77 emu/g to 59.55 emu/g, inset data in Fig. 8(a). Whereas, M_r and H_c at 10 K are in range (12.67–22.03) emu/g and (260–43) Oe, respectively. The increment at n_B values from 2.312 μ_B to 2.547 μ_B at 10 K with increasing content of Dy^{3+} was determined. Theoretical values of magnetic moments were calculated as increasing from 2.50 to 2.77 μ_B due to increasing Dy^{3+} content and in good accordance with the experimental

Table 2
Magnetic parameters of $Mn_{0.5}Zn_{0.5}Dy_xFe_{2-x}O_4$ (x ≤ 0.03) NPs at RT.

x	*Mw*	M_s *(emu/g)*	D_{mag} *(nm)*	n_B *(μ_B)*
0.00	235.74	22.51	15.64	0.952
0.01	236.80	22.56	15.97	0.954
0.02	237.87	24.25	19.0	1.032
0.03	238.93	26.59	20.87	1.137

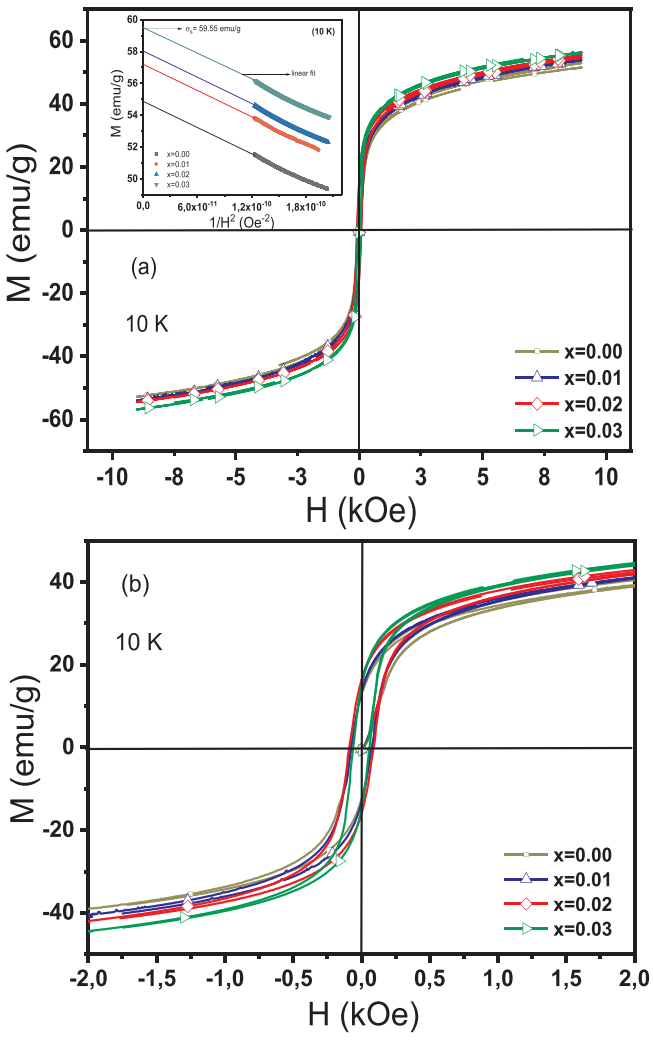

Fig. 8. Magnetic hysteresis curves of $Mn_{0.5}Zn_{0.5}Dy_xFe_{2-x}O_4$ (x ≤ 0.03) NPs (a) in magnetic field of ± 10 kOe, (b) in magnetic field of ± kOe at 10 K.

Table 3
Magnetic parameters of $Mn_{0.5}Zn_{0.5}Dy_xFe_{2-x}O_4$ (x ≤ 0.03) NPs at 10 K.

x	M_s (emu/g)	M_r (emu/g)	H_c (Oe)	n_B (μ_B)	n_B (μ_B), theo.	SQR M_r/M_s	K_{eff} (Erg/g)	H_a(Oe)
0.00	54.77	12.67	260	2.312	2.50	0.231	2.23×10^4	814.31
0.01	57.20	13.26	216	2.425	2.58	0.232	1.93×10^4	674.82
0.02	58.06	22.03	173	2.473	2.66	0.379	1.57×10^4	540.82
0.03	59.55	23.83	043	2.547	2.77	0.400	0.4×10^4	134.34

moment values as seen in Table 3. In addition to ion doping, increasing magnetization parameters at 10 K are mainly caused by excluded negative effects of heat [38,39]. In another words, there are too many new aligned spins to participate in the total magnetization [39]. In the literature, increments in M_s and M_r are also attributed to the growth in grain size, strengthening at super-exchange interactions and increasing the n_B [40,41].

The squareness ratio (SQR = M_r/M_s) was calculated for all samples. A theoretical limit of 0.50 determines single-domain structure with uniaxial anisotropy according to Stoner-Wohlfarth theory [35]. However, all samples have smaller SQR values (between 0.231 and 0.400) than theoretical limit at 10 K. Those significant variations confirm the multi-domain nature for samples [42,43]. Furthermore, H_c values at 10 K significantly decrease with increasing the ratio of Dy^{3+} that refer

to the influence of multi-domain nature and decreasing magneto-crystalline anisotropy [44]. We mentioned in Section 3.2 that average particle size is growing with increasing the Dy^{3+} content. Hence, larger particle size means more domain and more soft magnetic material with smaller coercivities and magneto-crystalline anisotropy.

The magnetic hardness of most NPs is due to the influence of magneto-crystalline anisotropy. In a multi-domain ferrite without any externally applied field, the magnetic moments are still precessing about the easy axis, which is the M_s direction, in each domain. The precession frequency depends on how strongly the magnetization is bound to the easy axis; the stronger the coupling, the higher is the natural frequency of precession. The strength of this coupling is described by the value of the magneto-crystalline anisotropy K or by the anisotropy field H_a, which is proportional to K.

Eq. (8) gives an expression between H_c, M_s and the effective magneto-crystalline anisotropy constant (K_{eff}) [45,46]:

$$H_c = 0.64\frac{K_{eff}}{M_s} \tag{8}$$

We employed Eq. (8) to estimate K_{eff} magnitudes for all products using 10 K magnetization data only since RT data do not have measured H_c magnitudes. All magnitudes are in the order of 10^3–10^4 Erg/g.

The $2K_{eff}$: M_s ratio is directly proportional to the magneto-crystalline anisotropy field as mentioned above [47,48]:

$$H_a = \frac{2K_{eff}}{M_s} \tag{9}$$

H_a values decrease from 814.31 Oe to 134.34 Oe with increasing Dy^{3+} content. All measured or calculated magnetic parameters from 10 K data are listed in Table 3. In Table 3, theoretical values of n_B were calculated by using the magnetic moment data belonging to each ion (by taking their alignment and concentrations into account) as stated by Cullity [48].

3.5.1. ZFC and FC measurements

Fig. 9(a) and (b) present ZFC and FC magnetization vs temperature (10–325 K) curves obtained at 100 Oe DC field for two selected $Mn_{0.5}Zn_{0.5}Dy_{0.01}Fe_{1.99}O_4$ and $Mn_{0.5}Zn_{0.5}Dy_{0.03}Fe_{1.97}O_4$ nanoparticle samples, respectively. Low field ZFC and FC measurements are applied to investigate the spin-glass or spin-glass-like phases as usual. It is clearly seen in both figures that curves separate at a temperature (bifurcation temperature), which is very near to peak temperature of the ZFC curves, indicating the collective spin-glass-like behavior below T_{peak} values [49,50].

Peak temperature values of ZFC magnetization curves occur at 71.2 and 78.8 K for both samples, respectively. Even FC curves exhibit a sharp drop below their T_{peak} positions. This is generally correlated to the collective freezing of system and assigned as proof of spin-glass-like phase [51]. However, spin-glass behavior requires the strong interactions between NPs. The higher ZFC peak temperature (78.8 K) belonging to $Mn_{0.5}Zn_{0.5}Dy_{0.03}Fe_{1.97}O_4$ which has higher Dy^{3+} concentration indicates, first of all, a higher intensity in interparticle interactions, since the ZFC maximum signals a “superspin glass” temperature determined by those interactions. These increasing interactions are due to larger size ferrite NPs [49]. To investigate the effective interactions in the nanoparticle powders in detail, reciprocal susceptibility (χ^{-1}) versus temperature graphs were plotted as shown in the insets of Fig. 9. Linear part of plots in high temperature region are extrapolated to $\chi^{-1} = 0$. The corresponding characteristic temperature, T_0 reflects qualitative measure of interparticle or intercluster interaction energy [51]. Estimated T_0 values are 207.2 K for $Mn_{0.5}Zn_{0.5}Dy_{0.01}Fe_{1.99}O_4$ and 253 K for $Mn_{0.5}Zn_{0.5}Dy_{0.03}Fe_{1.97}O_4$ NPs. Such high positive values are assigned as proof of strong magnetic especially ferromagnetic-like interactions [50–53]. T_0 increases drastically from 207.2 K to 253 K assigning the stronger ferromagnetic interactions for Dy^{3+} ion including mixed ferrite with x = 0.03. This determination in low temperature region is in well accordance with the 10 K VSM data as seen in Table 3.

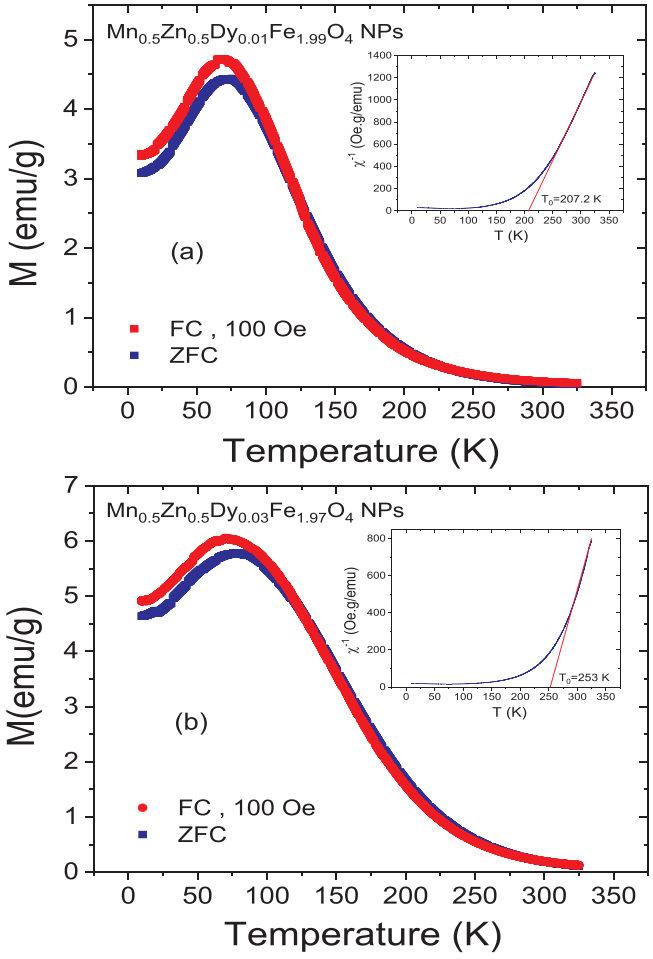

Fig. 9. ZFC-FC magnetization vs temperature curves for (a) $Mn_{0.5}Zn_{0.5}Dy_{0.01}Fe_{1.99}O_4$ and (b) $Mn_{0.5}Zn_{0.5}Dy_{0.03}Fe_{1.97}O_4$. The insets show the χ^{-1} vs T graphs for both samples.

3.5.2. AC susceptibility measurements

Fig. 10(a) and (b) display real parts of AC susceptibility (χ') measurements recorded from the selected $Mn_{0.5}Zn_{0.5}Dy_{0.01}Fe_{1.99}O_4$ and $Mn_{0.5}Zn_{0.5}Dy_{0.03}Fe_{1.97}O_4$ NPs, respectively. Five different applied frequencies range between 100 Hz and 10 kHz as noticeable in the figure. AC susceptibility measurements are usually conducted to analyze the dynamics of collective spin freezing in spin-glass samples in which temperature magnitude is associated with a maximum value of χ' and corresponds to spin freezing temperature (T_f). Peak temperature or spin freezing temperature positions vary marginally with respect to sharply increasing magnitude of measuring frequencies. This slight shift to higher temperature region is easily observed in the Fig. 10.

T_{peak} ($=T_f$) positions for $Mn_{0.5}Zn_{0.5}Dy_{0.01}Fe_{1.99}O_4$ NPs start from 74.80 K corresponding to 100 Hz and increases until 78.40 K corresponding to 100 kHz measuring frequency magnitudes. Similarly, T_{peak} positions for $Mn_{0.5}Zn_{0.5}Dy_{0.03}Fe_{1.97}O_4$ NPs increases from 94.30 K corresponding to 100–102.0 K corresponding to 100 kHz measuring frequency. The peak shift per frequency decade is quantified in the phenomenological parameter $c = \Delta T_p/(T_p \Delta \log f)$. The calculated c values are 0.0153 and 0.0252 for $Mn_{0.5}Zn_{0.5}Dy_{0.01}Fe_{1.99}O_4$ and for $Mn_{0.5}Zn_{0.5}Dy_{0.03}Fe_{1.97}O_4$ NPs, respectively. Those values are outside the expected range for superparamagnetic materials (c = 0.100–0.130) but in the range of many spin glass systems (c = 0.005–0.06), supporting the idea of spin-glass-like behavior for our NPs [51]. Further,

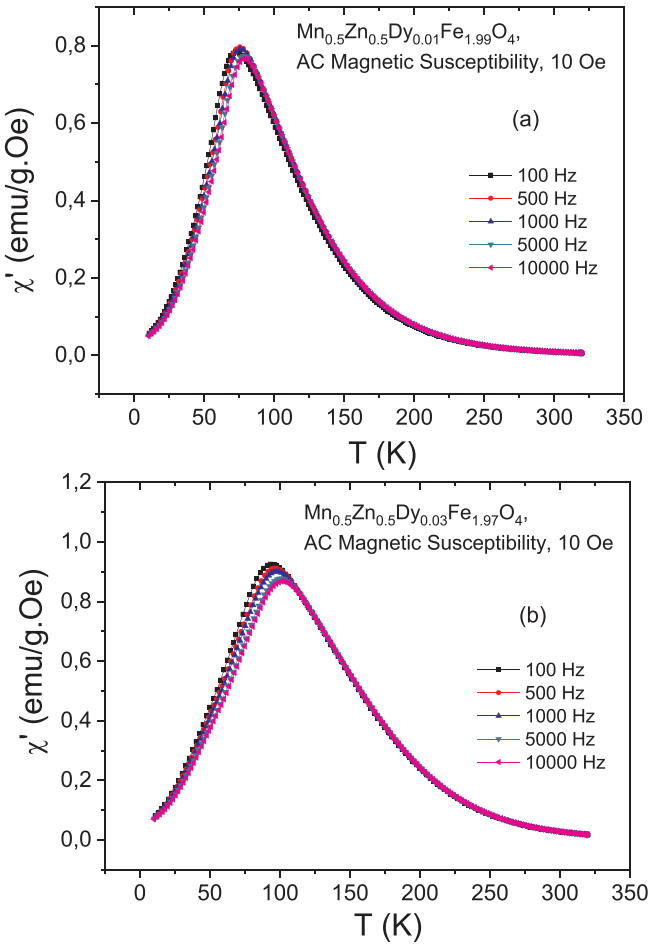

Fig. 10. Real part of AC susceptibility curves as function of temperature, $\chi'(T)$ for (a) $Mn_{0.5}Zn_{0.5}Dy_{0.01}Fe_{1.99}O_4$ and (b) $Mn_{0.5}Zn_{0.5}Dy_{0.03}Fe_{1.97}O_4$ NPs.

the intensity of peaks is higher for low measuring frequencies. Those entire characteristic features are observed not just at spin-glass but also at superparamagnetic systems [54–56].

In the last few decades, many models were developed to specify the AC susceptibility characteristics of magnetic NPs. The magnetic moment of superparamagnetic NPs has usually two stable orientations that are antiparallel to each other because of internal magnetic anisotropy. Those directions define the magnetic easy axis of nanoparticle and separated by an energy barrier, $E_a = K_{eff}V$, where V is the volume of nanoparticle. At finite temperature, there is a finite probability for the magnetization to flip and reverse its direction. The mean time between two flips is called the Néel relaxation time τ_N and is given by the Néel-Arrhenius equation. Hence, Néel -Arrhenius (N-A) model is consistent to analyze the independent or non-interacting particles and relates magnetic properties to anisotropy barrier and relaxation time ($\tau = 1/f$). E_a separates the magnetization reversal between two metastable states that arise from the spin frustration caused by the mixed valency in the system.

$$\tau = \tau_0 \exp\left[\frac{E_a}{k_B T_{peak}}\right] \tag{10}$$

where, the τ is the time between relaxation attempts, k_B is Boltzmann constant and τ_0 is a constant. By taking the natural logarithm of both sides in Eq. (10), we get,

$$ln\frac{1}{f} = ln\frac{1}{f_0} + \frac{E_a}{k_B T_{peak}} \tag{11}$$

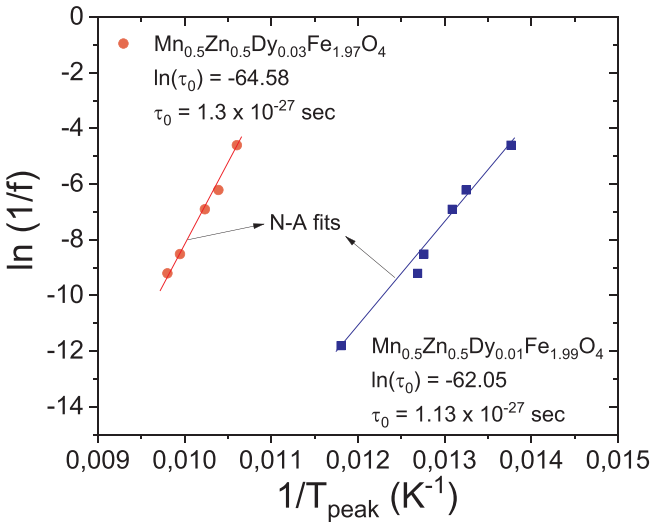

Fig. 11. ln(1/f) versus $1/T_{peak}$ plots and N-A fits for $Mn_{0.5}Zn_{0.5}Dy_{0.01}Fe_{1.99}O_4$ and $Mn_{0.5}Zn_{0.5}Dy_{0.03}Fe_{1.97}O_4$ NPs.

Fig. 11 shows the ln(1/f) versus $1/T_{peak}$ plots and N-A fits applying the Eq. (11). The intercept values ($\ln(\tau_0)$) are -62.05 and -64.58 belonging to both selected samples. Corresponding relaxation time constant, τ_0 magnitudes were intercepted as 1.13×10^{-27} s and 9.04×10^{-29} s. These magnitudes are unphysically small and show a fast divergence of response times with decreasing temperature. It is well known that for non-interacting particles that is for superparamagnetic systems relaxation times take values in a range $(10^{-9} - 10^{-12})$ s [51]. Hence, we can be sure that our selected samples do not exhibit a superparamagnetic behavior at low temperature region.

A collective glassy magnetic state might occur in ensembles of single domain nanoparticles in that the interparticle interactions are effective. A magnetic sample which exhibits spin-glass-like transition is supposed to show critical slowing down (CSD) and characteristic relaxation time τ correlates with T according to formula of CSD model [56],

$$\tau = \tau_0 \left[\frac{T_f}{T_g} - 1\right]^{-z\vartheta} \tag{12}$$

where $T_f$had been defined as spin freezing temperature, T_g is spin-glass transition temperature, $z\vartheta$ is the dynamic critical exponent and varies between 4 and 12 representing the strength of magnetic interaction. If we take the logarithm of both sides of Eq. (12), we get,

$$log\tau = log\tau_0 - z\vartheta log\left[\frac{T_f}{T_g} - 1\right] \tag{13}$$

Fig. 12 shows the $log\tau = log\frac{1}{f}$ versus $\log\left[\frac{T_f}{T_g} - 1\right]$ plots and CSD fits for two selected samples applying the Eq. (13). Employing T_g as fit parameter, the best fit of equation yields the data $log\tau_0 = -12.98$, $\tau_0 = 1.047 \times 10^{-13}$s, $z\vartheta = 10.0$ and $T_g = 69,45K$ for $Mn_{0.5}Zn_{0.5}Dy_{0.01}Fe_{1.99}O_4$ NPs. Similarly, we obtained the best fit data for $Mn_{0.5}Zn_{0.5}Dy_{0.03}Fe_{1.97}O_4$ NPs as $log\tau_0 = -10.30$, $\tau_0 = 5.02 \times 10^{-11}$s, $z\vartheta = 11.2$ and $T_g = 79.90K$. We can easily notice that $z\vartheta$ values of both samples are in the typical range of [4–12] and are close to the value of a 3D Ising spin glass [57,58]. Spin flip time values of 1.047×10^{-13}s and 5.02×10^{-11}s are also in the typical range between 10^{-9} and 10^{-13} s for 3D frustrated systems like spin-glasses [57,58].

4. Conclusion

Nanoparticles of $Mn_{0.5}Zn_{0.5}Dy_xFe_{2-x}O_4$ ($x \leq 0.03$) were prepared by using Ultrasonic irradiation. XRD, SEM, TEM and FTIR confirmed the formation of doped Mn-Zn ferrites. Replacement of Dy^{3+} for Fe^{3+}

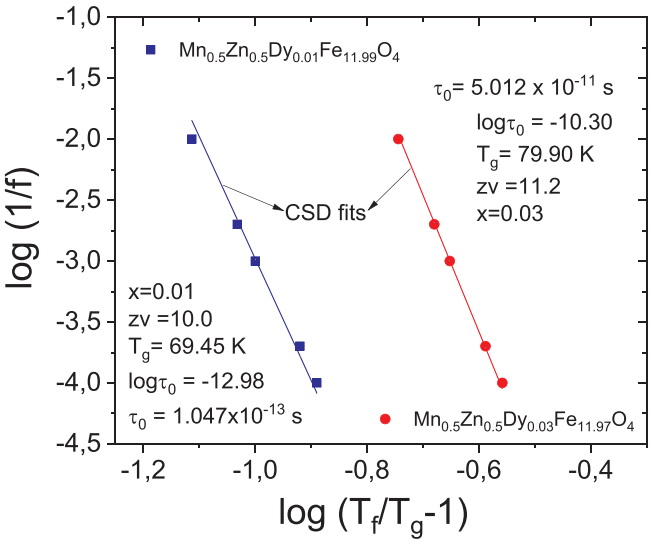

Fig. 12. Analysis of CSD of the relaxation time for $Mn_{0.5}Zn_{0.5}Dy_{0.01}Fe_{1.99}O_4$ and $Mn_{0.5}Zn_{0.5}Dy_{0.03}Fe_{1.97}O_4$ NPs.

ions with increasing the ratio causes to lattice micro-strains due to larger ionic radius. SEM images revealed a regular size and uniform distribution of cubic particles. TEM images of $Mn_{0.5}Zn_{0.5}Dy_xFe_{2-x}O_4$ (x = 0.01 and 0.02) NPs showed an agglomeration of cubic nanoparticles due to magnetic interaction among them. PDR measurements revealed the strong light absorption in the UV–vis region. Estimated direct E_g magnitudes, which are in the semiconductor band-gap range for whole products, did not change significantly because of Dy^{3+} ions doping. RT magnetization curves and 10 K DC field hysteresis loops exhibit the superparamagnetic and the ferrimagnetic features of all measured samples, respectively. About increasing magnetization, VSM results are consistent with the theoretical magnetic moment increment due to Dy^{3+} ion substitution. SQRs calculated using 10 K magnetization data are smaller than the theoretical limit of 0.50 and point to the multi-domain structure for all NPs. The replacement of dopant ions with Fe^{3+} causes to decrement in intrinsic anisotropy field and coercivity magnitudes. Again, at 10 K, the replacement of dopant Dy^{3+} ions with Fe^{3+} causes to decrease in H_a and H_c magnitudes. The extrapolated very high characteristic temperature, T_0 values of 207.2 K and 253 K from ZFC and FC measurements reveal the existence of interparticle ferromagnetic-like interactions. Higher Dy^{3+} including sample has the higher interparticle interaction. CSD model explains the frequency dependent AC susceptibility data consistently. That is, characteristic relaxation time τ correlates with T providing meaningful physical data. The phenomenological c parameter values of 0.0153 and 0.0252 belonging to $Mn_{0.5}Zn_{0.5}Dy_xFe_{2-x}O_4$ (x = 0.01 and 0.03) samples supported the idea of spin-glass-like behavior for our doped NPs. The theoretically estimated data, such as $z\vartheta$ values of 10.0 and 11.2 and τ_0 values of 1.047×10^{-13}s and 5.02×10^{-11}s are assigned to 3D frustrated systems proving the spin-glass-like behavior of mixed ferrites doped by Dy^{3+} ions at low temperatures.

Declaration of Competing Interest

The authors declare that they have no known competing financial interests or personal relationships that could have appeared to influence the work reported in this paper.

References

[1] H. Waqas, A.H. Qureshi, K. Subhan, M. Shahzad, Nanograin Mn–Zn ferrite smart cores to miniaturize electronic devices, Ceram. Int. 38 (2012) 1235–1240.

[2] K. Praveena, K. Sadhana, S. Bharadwaj, S. Murthy, Development of nanocrystalline Mn–Zn ferrites for high frequency transformer applications, J. Magn. Magn. Mater. 321 (2009) 2433–2437.

[3] K. Pubby, S.B. Narang, Influence of grain size and porosity on X-band properties of Mn-Zr substituted Ni-Co ferrites, Mater. Lett. 244 (2019) 186–191.

[4] K. Pubby, S.B. Narang, Ka band absorption properties of substituted nickel spinel ferrites: comparison of open-circuit approach and short-circuit approach, Ceram. Int. (2019), https://doi.org/10.1016/j.ceramint.2019.08.081.

[5] K. Praveena, K. Sadhana, S. Bharadwaj, S. Murthy, Development of NANOCRYSTALLINE Mn–Zn Ferrites for Forward Type DC–DC Converter for Switching Mode Power Supplies, Taylor & Francis, 2010.

[6] K. Praveena, K. Sadhana, S. Bharadwaj, S. Murthy, Fabrication of dc–dc converter using nanocrystalline Mn–Zn ferrites, Mater. Res. Innovations 14 (2010) 102–106.

[7] R. Huang, D. Zhang, K.-J. Tseng, Determination of dimension-independent magnetic and dielectric properties for Mn–Zn ferrite cores and its EMI applications, IEEE Trans. Electromagn. Compat. 50 (2008) 597–602.

[8] Z. Beji, M. Sun, L. Smiri, F. Herbst, C. Mangeney, S. Ammar, Polyol synthesis of non-stoichiometric Mn–Zn ferrite nanocrystals: structural/microstructural characterization and catalytic application, RSC Adv. 5 (2015) 65010–65022.

[9] T. Xie, H. Li, C. Liu, J. Yang, T. Xiao, L. Xu, Magnetic photocatalyst $BiVO_4$/Mn-Zn ferrite/reduced graphene oxide: synthesis strategy and its highly photocatalytic activity, Nanomaterials 8 (2018) 380.

[10] C.Q. Shen, H.N. Ji, J. Wu, N. Zhu, J.Q. Niu, H.D. Li, X.B. Niu, Synthesis and characterization of MnZn Ferrite Nanoparticles for Biomedical Applications, 2018 IEEE International Conference on Applied Superconductivity and Electromagnetic Devices (ASEMD), IEEE, 2018, pp. 1–2.

[11] S. Amiri, H. Shokrollahi, Magnetic and structural properties of RE doped Co-ferrite (RE = Nd, Eu, and Gd) nano-particles synthesized by co-precipitation, J. Magn. Magn. Mater. 345 (2013) 18–23.

[12] X.C. Zhong, X.J. Guo, S.Y. Zou, H.Y. Yu, Z.W. Liu, Y.F. Zhang, K.X. Wang, Improving soft magnetic properties of Mn-Zn ferrite by rare earth ions doping, AIP Adv. 8 (2017) 047807.

[13] V.J. Angadi, L. Choudhury, K. Sadhana, H.-L. Liu, R. Sandhya, S. Matteppanavar, B. Rudraswamy, V. Pattar, R.V. Anavekar, K. Praveena, Structural, electrical and magnetic properties of Sc^{3+} doped Mn-Zn ferrite nanoparticles, J. Magn. Magn. Mater. 424 (2017) 1–11.

[14] P. Thakur, R. Sharma, M. Kumar, S. Katyal, N. Negi, N. Thakur, V. Sharma, P. Sharma, Superparamagnetic La Doped Mn-Zn Nano Ferrites: Dependence on Dopant Content and Crystallite Size, (2016).

[15] P.P. Goswami, H.A. Choudhury, S. Chakma, V.S. Moholkar, Sonochemical synthesis and characterization of manganese ferrite nanoparticles, Ind. Eng. Chem. Res. 52 (2013) 17848–17855.

[16] M. Ahmed, S. Ramulu Torati, B. Parvatheeswara Rao, M. Abdel Hamed, C. Kim, Size controlled sonochemical synthesis of highly crystalline superparamagnetic Mn–Zn ferrite nanoparticles in aqueous medium, J. Alloys Compd. 644 (2015) 774–782.

[17] M. Abdellatif, A. Azab, M. Salerno, Effect of rare earth doping on the vibrational spectra of spinel Mn-Cr ferrite, Mater. Res. Bull. 97 (2018) 260–264.

[18] E. Hannachi, M.A. Almessiere, Y. Slimani, A. Baykal, F. Ben, Azzouz, AC susceptibility investigation of YBCO superconductor added by carbon nanotubes, J. Alloys Compd. 812 (2020) 152150.

[19] S.E. Shirsath, M. Mane, Y. Yasukawa, X. Liu, A. Morisako, Chemical tuning of structure formation and combustion process in $CoDy_{0.1}Fe_{1.9}O_4$ nanoparticles: influence@ pH, J. Nanopart. Res. 15 (2013) 1976.

[20] S.E. Shirsath, M.L. Mane, Y. Yasukawa, X. Liu, A. Morisako, Self-ignited high temperature synthesis and enhanced super-exchange interactions of Ho^{3+}–Mn^{2+}–Fe^{3+}–O^{2-} ferromagnetic nanoparticles, Phys. Chem. Chem. Phys. 16 (2014) 2347–2357.

[21] S.E. Shirsath, D. Wang, S.S. Jadhav, M.L. Mane, S. Li, Ferrites obtained by sol-gel method, in: L. Klein, M. Aparicio, A. Jitianu (Eds.), Handbook of Sol-Gel Science and Technology: Processing, Characterization and Applications, Springer International Publishing, Cham, 2018, pp. 695–735.

[22] T. Dippong, I.G. Deac, O. Cadar, E.A. Levei, L. Diamandescu, G. Borodi, Effect of Zn content on structural, morphological and magnetic behavior of $Zn_xCo_{1-x}Fe_2O_4/SiO_2$ nanocomposites, J. Alloys Compd. 792 (2019) 432–443.

[23] K. Pubby, S.S. Meena, S.M. Yusuf, S.B. Narang, Cobalt substituted nickel ferrites via Pechini's sol–gel citrate route: X-band electromagnetic characterization, J. Magn. Magn. Mater. 466 (2018) 430–445.

[24] J.P. Blitz, Diffuse reflectance spectroscopy, Modern Techniques in Applied Molecular Spectroscopy, 1998, p. 185.

[25] J. Tauc, R. Grigorovici, A. Vancu, Optical properties and electronic structure of amorphous germanium, Phys. Status Solidi (B) 15 (1966) 627–637.

[26] M.A. Almessiere, Y. Slimani, S. Güner, M. Nawaz, A. Baykal, F. Aldakheel, S. Akhtar, I. Ercan, İ. Belenli, B. Ozçelik, Magnetic and structural characterization of Nb^{3+}-substituted $CoFe_2O_4$ nanoparticles, Ceram. Int. 45 (2019) 8222–8232.

[27] A. Baykal, S. Esir, A. Demir, S. Güner, Magnetic and optical properties of $Cu_{1-x}Zn_xFe_2O_4$ nanoparticles dispersed in a silica matrix by a sol–gel auto-combustion method, Ceram. Int. 41 (2015) 231–239.

[28] P. Nam, N. Phuc, P. Linh, L. Lu, D. Manh, P. Phong, I.-J. Lee, Effect of zinc on structure, optical and magnetic properties and magnetic heating efficiency of $Mn_{1-x}Zn_xFe_2O_4$ nanoparticles, Phys. B 550 (2018) 428–435.

[29] A. Ashok, L.J. Kennedy, J.J. Vijaya, Structural optical and magnetic properties of $Zn_{1-x}Mn_xFe_2O_4$ ($0 \leq x \leq 0.5$) spinel nano particles for transesterification of used cooking oil, J. Alloys Compd. 780 (2019) 816–828.

[30] A. Baykal, S. Güner, A. Demir, Synthesis and magneto-optical properties of triethylene glycol stabilized $Mn_{1-x}Zn_xFe_2O_4$ nanoparticles, J. Alloys Compd. 619 (2015) 5–11.

[31] A. Demir, S. Güner, Y. Bakis, S. Esir, A. Baykal, Magnetic and optical properties of

$Mn_{1-x}Zn_xFe_2O_4$ nanoparticles, J. Inorg. Org. Poly. Mater. 24 (2014) 729–736.
[32] A. Baykal, S. Güner, A. Demir, S. Esir, F. Genç, Effect of zinc substitution on magneto-optical properties of $Mn_{1-x}Zn_xFe_2O_4/SiO_2$ nanocomposites, Ceram. Int. 40 (2014) 13401–13408.
[33] K. Lopez-Maldonado, P. De la Presa, I. Betancourt, J.F. Mancilla, J.M. Aquino, A. Hernando, J.E. Galindo, Superparamagnetic response of zinc ferrite incrusted nanoparticles, J. Alloys Compd. 637 (2015) 443–448.
[34] X. Li, Y. Hou, Q. Zhao, L. Wang, A general, one-step and template-free synthesis of sphere-like zinc ferrite nanostructures with enhanced photocatalytic activity for dye degradation, J. Colloid Interf. Sci. 358 (2011) 102–108.
[35] E.C. Stoner, E. Wohlfarth, A mechanism of magnetic hysteresis in heterogeneous alloys, Philos. Trans. Royal Soc. London Series A, Math. Phys. Sci. 240 (1948) 599–642.
[36] L. Zhao, H. Yang, L. Yu, Y. Cui, X. Zhao, S. Feng, Magnetic properties of Re-substituted Ni–Mn ferrite nanocrystallites, J. Mater. Sci. 42 (2007) 686–691.
[37] K. Yakushiji, S. Mitani, K. Takanashi, J.-G. Ha, H. Fujimori, Composition dependence of particle size distribution and giant magnetoresistance in Co–Al–O granular films, J. Magn. Magn. Mater. 212 (2000) 75–81.
[38] K. Zipare, S. Bandgar, G. Shahane, Effect of Dy-substitution on structural and magnetic properties of MnZn ferrite nanoparticles, J. Rare Earths 36 (2018) 86–94.
[39] Y. Slimani, M. Almessiere, S. Güner, N. Tashkandi, A. Baykal, M. Sarac, M. Nawaz, I. Ercan, Calcination effect on the magneto-optical properties of vanadium substituted $NiFe_2O_4$ nanoferrites, J. Mater. Sc.: Mater. Electr. 30 (2019) 9143–9154.
[40] M. Amir, H. Gungunes, Y. Slimani, N. Tashkandi, H. El Sayed, F. Aldakheel, M. Sertkol, H. Sozeri, A. Manikandan, I. Ercan, Mössbauer studies and magnetic properties of cubic $CuFe_2O_4$ nanoparticles, J. Supercond. Novel Magn. 32 (2019) 557–564.
[41] M. Almessiere, Y. Slimani, S. Güner, A. Baykal, I. Ercan, Effect of dysprosium substitution on magnetic and structural properties of $NiFe_2O_4$ nanoparticles, J. Rare Earths (2019).
[42] T.H. Mubarak, O.A. Mahmood, Z.J. Hamakhan, Structural, magnetic and electrical properties of $Ba_2Mg_2Fe_{28}O_{46}$ (Mg2X) hexaferrites, Int. J. Appl. Eng. Res. 13 (2018) 6369–6379.
[43] M.N. Ashiq, R.B. Qureshi, M.A. Malana, M.F. Ehsan, Synthesis, structural, magnetic and dielectric properties of zirconium copper doped M-type calcium strontium hexaferrites, J. Alloys Compd. 617 (2014) 437–443.
[44] M. Almessiere, Y. Slimani, S. Ali, A. Baykal, I. Ercan, H. Sozeri, Nd^{3+} ion-substituted $Co_{1-2x}Ni_xMn_xFe_{2-y}Nd_yO_4$ nanoparticles: structural, morphological, and magnetic investigations, J. Inorg. Org. Poly. Mater. 29 (2019) 783–791.
[45] M. Sadat, R. Patel, J. Sookoor, S.L. Bud'ko, R.C. Ewing, J. Zhang, H. Xu, Y. Wang, G.M. Pauletti, D.B. Mast, Effect of spatial confinement on magnetic hyperthermia via dipolar interactions in Fe_3O_4 nanoparticles for biomedical applications, Mater. Sci. Eng.: C 42 (2014) 52–63.
[46] M. Amir, M. Geleri, S. Güner, A. Baykal, H. Sözeri, Magneto optical properties of $FeB_xFe_{2-x}O_4$ nanoparticles, J. Inorg. Org. Poly. Mater. 25 (2015) 1111–1119.
[47] S. Asiri, S. Güner, A. Korkmaz, M. Amir, K. Batoo, M. Almessiere, H. Gungunes, H. Sözeri, A. Baykal, Magneto-optical properties of $BaCr_yFe_{12-y}O_{19}$ ($0.0 \leq y \leq 1.0$) hexaferrites, J. Magn. Magn. Mater. 451 (2018) 463–472.
[48] B.D. Cullity, C.D. Graham, Introduction to Magnetic Materials, John Wiley & Sons, Hoboken, NJ, USA, 2011.
[49] J.A. Mydosh, Spin Glasses: An Experimental Introduction, Taylor & Francis, London; Washington, DC, 1993.
[50] J. Du, B. Zhang, R. Zheng, X. Zhang, Memory effect and spin-glass-like behavior in Co-Ag granular films, Phys. Rev. B 75 (2007) 014415.
[51] H. Khurshid, P. Lampen-Kelley, Ò. Iglesias, J. Alonso, M.-H. Phan, C.-J. Sun, M.-L. Saboungi, H. Srikanth, Spin-glass-like freezing of inner and outer surface layers in hollow γ-Fe_2O_3 nanoparticles, Sci. Rep. 5 (2015) 15054.
[52] M. Almessiere, Y. Slimani, H. El Sayed, A. Baykal, Ce-Y co-substituted strontium nanohexaferrites: AC susceptibility and Mossbauer studies, Cer. Int. 44 (2018) 12520–12527.
[53] M. Almessiere, Y. Slimani, H. Güngüneş, H. El Sayed, A. Baykal, AC susceptibility and Mossbauer study of Ce^{3+} ion substituted $SrFe_{12}O_{19}$ nanohexaferrites, Ceram. Int. 44 (2018) 10470–10477.
[54] J. Dormann, D. Fiorani, E. Tronc, On the models for interparticle interactions in nanoparticle assemblies: comparison with experimental results, J. Magn. Magn. Mater. 202 (1999) 251–267.
[55] S. Dhar, O. Brandt, A. Trampert, K. Friedland, Y. Sun, K. Ploog, Observation of spin-glass behavior in homogeneous (Ga, Mn) N layers grown by reactive molecular-beam epitaxy, Phys. Rev. B 67 (2003) 165205.
[56] M. Hakim, M.M. Haque, M. Huq, P. Nordblad, Spin-glass-like ordering in the spinel $ZnFe_2O_4$ ferrite, Phys. B 406 (2011) 48–51.
[57] Y. Slimani, A. Baykal, A. Manikandan, Effect of Cr^{3+} substitution on AC susceptibility of Ba hexaferrite nanoparticles, J. Magn. Magn. Mater. 458 (2018) 204–212.
[58] K. Gunnarsson, P. Svedlindh, P. Nordblad, L. Lundgren, H. Aruga, A. Ito, Dynamics of an Ising spin-glass in the vicinity of the spin-glass temperature, Phys. Rev. Lett. 61 (1988) 754.